ACS APPLIED MATERIALS & INTERFACES

www.acsami.org

Research Article

Carbon Nanoparticles–Fe(II) Complex for Efficient Tumor Inhibition with Low Toxicity by Amplifying Oxidative Stress

Ping Xie, Sheng-Tao Yang,* Yuanfang Huang, Cheng Zeng, Qian Xin, Guangfu Zeng, Shengnan Yang, Pingfang Xia, Xiaohai Tang,* and Kexin Tang

Cite This: *ACS Appl. Mater. Interfaces* 2020, 12, 29094–29102

Read Online

ACCESS | Metrics & More | Article Recommendations | Supporting Information

ABSTRACT: The Fe element is essential for human beings, but overdose of Fe leads to unwanted toxicity. However, overwhelming Fe accumulation in tumor cells could arouse strong oxidative stress for cancer therapy. Therefore, the fast and specific accumulation of Fe in tumor cells without systemic toxicity is critical for this purpose. Herein, we report that a carbon nanoparticles–Fe(II) complex (CNSI–Fe) could efficiently load Fe into tumor cells and inhibit tumor growth with low toxicity in H22 tumor-bearing mice. Upon intratumoral injection, CNSI–Fe only induced meaningful Fe increase in the tumor to significantly inhibit tumor growth with competitive efficiency to *cis*-dichlorodiammineplatinum(II). Fe accumulation stimulated the hydroxyl radical generation and serious oxidative stress in the tumor. Due to the lack of Fe accumulation in other tissues, CNSI–Fe was of low systemic toxicity to tumor-bearing mice. With the clinical success of CNSI for decades, CNSI–Fe might be used for cancer therapy through "off label" use to benefit patients immediately.

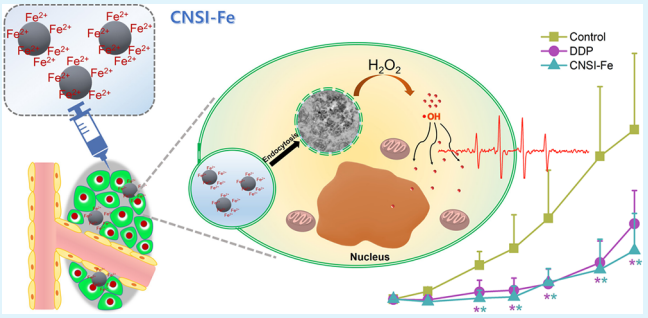

KEYWORDS: *carbon nanoparticles, ferrous ion, tumor inhibition, oxidative stress, toxicity*

INTRODUCTION

Fe is an essential element for human beings.[1] Fe is necessary for hemoglobin, myohemoglobin, cytochrome oxidase, and so on. Fe is crucial for hematopoiesis, immunologic function, and absorption of Zn element. There is a well-established Fe balance in the body to maintain the required Fe concentration. Fe could be transported into cytoplasm by transferrin (Tf)–Fe2/Tf receptor (TFR) endocytosis and other Tf-independent pathways.[2] Fe could be exported through ferroportin (FPN) to maintain the system iron homeostasis.[3] However, when overwhelming Fe ions are present in the cytoplasm, cells are incapable to pump out Fe ions in time and cytotoxicity would occur. It is well known that Fe^{2+} is highly catalytically reactive in the decomposition of H_2O_2 to produce hydroxyl radicals, namely, Fenton reaction.[4] When overwhelming Fe^{2+} is present in tissues, Fe^{2+} would catalyze the in vivo decomposition of H_2O_2 and lead to strong oxidative stress. This process has been widely acknowledged in the toxicity evaluations of Fe and Fe-containing materials.[5,6]

In recent decades, the tumor microenvironment (TME) is recognized as a useful target for cancer therapy.[7,8] TME-responsive drugs are developed for this purpose. Among these TME drugs, there are rapid achievements in reactive oxygen species (ROS) generation reagents and techniques.[9−12] For example, tirapazamine,[9] doxorubicin,[10] photodynamic therapy,[11] and radiotherapy[12] are capable of generating ROS to kill tumors. In TME, there is a H_2O_2 overproduction; therefore, Fe^{2+} could catalyze the decomposition of H_2O_2 to produce hydroxyl radicals.[13] Another privilege of using Fe^{2+} for this purpose is that tumor cells upregulate the Fe uptake-related pathways and block Fe exportation of the FPN pathway.[2,3] Unfortunately, direct injection of Fe^{2+} is not suitable for in vivo treatment, because Fe^{2+} migrates along the blood circulation fast and free Fe^{2+} is highly toxic to the body.[14] Therefore, Fe should be used in a suitable formulation for tumor therapy.

Many Fe-containing nanomaterials have been reported to induce ROS generation and ferroptosis for tumor inhibition.[15−19] Such attempts broadened the applications of the Fe element in cancer therapy. For example, Liu et al. used FeP nanoparticles with ultrasound and photothermal-enhanced Fenton properties for cancer therapy, where the generation of hydroxyl radicals was achieved under irradiation of ultrasound or near-infrared (NIR) II light.[16] Gao et al. achieved nanocatalytic tumor therapy by Au and Fe_3O_4 nanoparticles to produce H_2O_2 and generate hydroxyl

Received: April 26, 2020
Accepted: June 8, 2020
Published: June 8, 2020

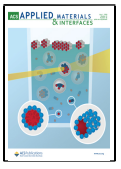

https://dx.doi.org/10.1021/acsami.0c07617
ACS Appl. Mater. Interfaces 2020, 12, 29094–29102

radicals.[17] To enhance the therapeutic effect of Fe-containing nanoparticles, many studies have used photothermal therapy, an external magnetic field, and the NIR-assisted Fenton reaction during treatment.[15,18] However, Fe-containing nanoparticles usually have a lower efficiency than Fe^{2+} in catalyzing the Fenton reaction.

Carbon nanoparticles suspension injection (CNSI) is the only commercialized and clinically applied carbon nanomaterials.[20,21] CNSI is applied in staining the tumor drainage lymph nodes black before surgery of advanced gastric cancer, breast cancer, and papillary thyroid carcinoma. There are many oxygen-containing groups on CNSI that could interact with Fe^{2+} and during endocytosis of the Fe^{2+} solution could be sucked into the cytoplasm. Thus, CNSI might be used as a carrier for Fe^{2+} for antitumor therapy. Beyond that, CNSI is of very low systemic toxicity according to animal experiments and clinical observations.[22] Annually, more than 100 000 patients are using CNSI during oncological surgery. Therefore, CNSI−Fe holds great advantage over other nanomaterials for clinical applications as it would be immediately accessible for cancer patients through "off label" use.

In this study, we intratumorally injected CNSI−Fe to achieve efficient tumor growth inhibition with low toxicity in H22 tumor-bearing mice. Tumor growth was monitored, and tumor tissues were checked by hematoxylin−eosin (HE) staining, immunohistochemistry, and transmission electron microscopy (TEM). Retention of CNSI−Fe in the tumor was quantified by Prussian blue staining, inductively coupled plasma-optical emission spectrometry (ICP-OES), and isotope ratio mass spectrometry (IRMS). Generation of hydroxyl radicals was monitored by electron spin-resonance spectroscopy (ESR), and the oxidative stress was measured. The toxicity of CNSI−Fe was evaluated by bodyweight increase, hematology, serum biochemistry, and histopathology. The implications to the clinical applications of CNSI−Fe are discussed.

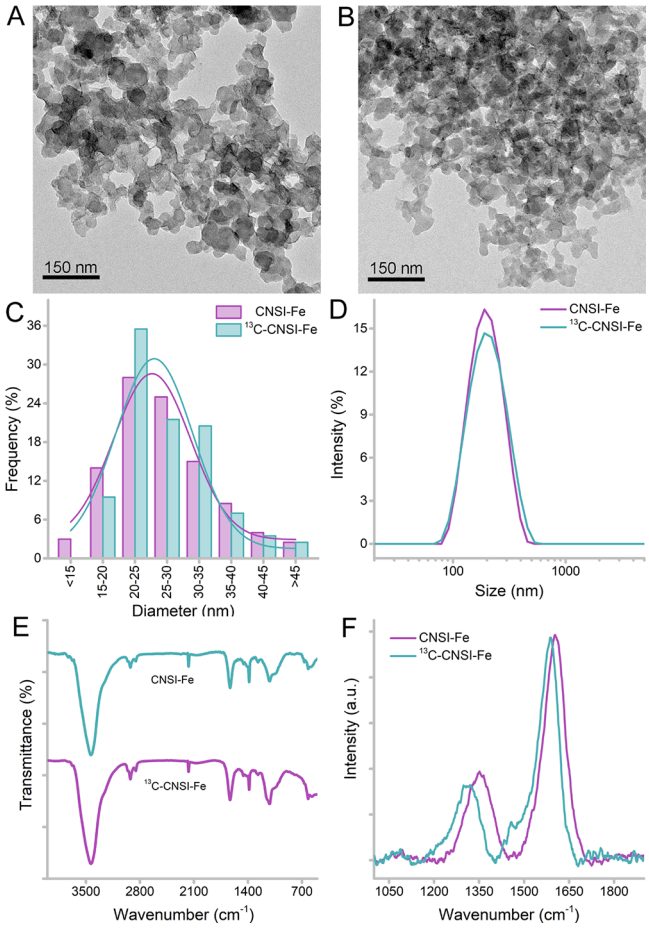

Figure 1. Characterization of CNSI−Fe and ^{13}C-CNSI−Fe. (A) TEM image of CNSI−Fe. (B) TEM image of ^{13}C-CNSI−Fe. (C) Particle size counts from TEM images. (D) Dynamic light scattering (DLS) spectra. (E) IR spectra; (F) Raman spectra.

RESULTS

Characterization of CNSI−Fe and ^{13}C-CNSI−Fe. CNSI was a black suspension of carbon nanoparticles prepared by dispersing carbon ash with polyvinylpyrrolidone (PVP) (Figure S1). After adding Fe^{2+}, the appearance did not change. CNSI−Fe was a black and stable aqueous dispersion for more than 6 months. The quality and purity of CNSI−Fe and ^{13}C-CNSI−Fe samples were carefully characterized using several techniques (Figure 1).[22] Under TEM, both samples were aggregated small nanoparticles, which were embedded in PVP during the drying process of sampling (Figure 1A and 1B and Figure S2). Fe^{2+} was homogeneously distributed and thus not recognizable. By counting the diameter of the particles, CNSI−Fe (27.2 ± 7.6 nm) and ^{13}C-CNSI−Fe (27.4 ± 6.8 nm) shared similar distribution patterns. In aqueous solution, the hydrodynamic radii were both centered at 190 nm, only 1 nm larger than that of CNSI without Fe (189 nm). In the infrared (IR) spectra, the oxygen-containing groups were identified at 3441 (−OH) and 1111 cm^{-1} (C−O). The peaks at 2924 and 2855 cm^{-1} were assigned to C−H, and the peak at 1631 cm^{-1} was attributed to aromatic C═C. The presence of O and H was also observed in elemental analysis (C, 59.4%; H, 2.4%; O, 19.3%; N, 2.4%; S, 2.9%). The sp^2 C domain was confirmed by the G band (1601 cm^{-1}) in the Raman spectra. The shift of the G band toward lower wavenumber at 1587 cm^{-1} was due to the isotope labeling on the skeleton in the ^{13}C-CNSI−Fe sample. In addition, the strong binding Fe^{2+} on CNSI was only a small portion (7.3%). Most of the Fe^{2+} (higher than 98%) was stable against oxidation, which was vital for the Fenton reaction. Overall, the characterization data collectively suggested that CNSI−Fe and ^{13}C-CNSI−Fe were suitable for the following animal treatments and evaluations.

Tumor Growth Inhibition. After intratumoral injection to H22-bearing mice, CNSI−Fe significantly inhibited tumor growth during the observation period of 14 days (Figure 2). Tumor growth was significantly inhibited after 5 days postinjection. Tumor volume was 1174 mm^3 for the control group, 415 mm^3 for the CNSI−Fe-treated group, and 583 mm^3 for the *cis*-dichlorodiammineplatinum(II) (DDP)-treated group. Correspondingly, the inhibition efficiency was 64.7% for CNSI−Fe and 50.3% for DDP. It should be noted that equivalent CNSI alone had no therapeutic effect (−3.1% for the CNSI group), and equivalent Fe^{2+} was much less efficient [31.9% for the Fe(II) group] (Figure S3). After sacrifice at 14 days, the tumor weights were 1.09 g for the control group, 0.58 g for the DDP-treated group, and 0.44 g for the CNSI−Fe-treated group. The inhibition efficiency was 59.6% for CNSI−Fe and 46.8% for DDP. Therefore, CNSI−Fe was competitive with the classical antitumor drug DDP for cancer therapy. A large area of necrosis (yellow arrows in Figure 2 C) was observed in the HE image of the CNSI−Fe-treated group, while the tumor tissue kept the normal structure in the control

https://dx.doi.org/10.1021/acsami.0c07617
ACS Appl. Mater. Interfaces 2020, 12, 29094−29102

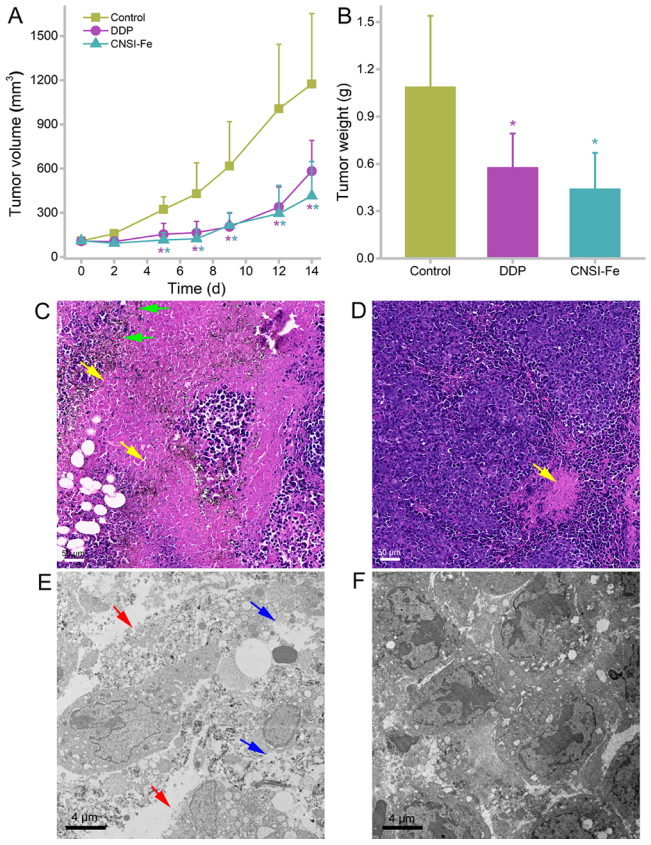

Figure 2. Tumor growth inhibition by CNSI–Fe. (A) Tumor volume. (B) Tumor weight. (C) HE image of CNSI–Fe-treated tumor. (D) HE image of the tumor in the control group. (E) TEM image of CNSI–Fe-treated tumor. (F) TEM image of the tumor in the control group. (*) $p < 0.05$ compared with the control group ($n = 5$). Green arrows (C) indicate the brown CNSI, yellow arrows (C, D) indicate the necrosis of tumor tissues, red arrows (E) indicate the broken cell membrane, and blue arrows (E) indicate loss of cytoplasm.

group with very limited necrosis area. The areas of necrosis were small in the CNSI group and Fe(II) group too (Figure S3). It could be clearly seen in the TEM image that the cellular structure of the CNSI–Fe-treated group was destroyed. The membrane was broken (red arrows in Figure 2E), and the cytoplasm was lost (blue arrows in Figure 2E). Further immunohistochemical analyses indicated that CNSI–Fe injection led to apoptosis of tumor cells (Figure 3). The areal density of the CNSI–Fe group was 0.071, three times that of the control group (0.023). The CNSI group, Fe(II) group, and DDP group also slightly increased the caspase 3 levels. In the proliferation indicator Ki67 analyses, no increase was observed in the CNSI–Fe group. The was also the case for the other three groups. The tumor growth measurements and structural observations suggested that CNSI–Fe was efficient in cancer therapy.

Fe Accumulation in the Tumor. Tumor inhibition by CNSI–Fe was mainly due to Fe accumulation. To verify Fe accumulation in tumor tissues, we stained the tumor sections with Prussian blue. The intratumoral injection of CNSI–Fe largely increased the Fe contents in the tumor tissues (Figure 4). The distribution of Fe was heterogeneous in the tumor tissues. The blue color of Prussian blue and black color of CNSI merged well, which interfered with the observation. In the blue stained area, the cellular structure was destroyed and the necrosis was more serious. At the edge of the dark stained area (containing CNSI and Prussian blue), the blue color could be clearly recognized. In the continuous sliced samples that were separately stained by Prussian blue and HE (the slices looked similar but could not be identical), we could roughly assign the blue stained area to tumor cells. The blue color was easier to distinguish in the Fe(II) group, where the blue stained area was assigned to tumor cells too. In contrast, the control group and the CNSI group were not stained blue (Figure S4), suggesting a low Fe concentration in tumor tissues without Fe injection. Typically, cells have specific pathways to balance the Fe concentration. However, the coexposure of CNSI and Fe might lead to more endocytosis. CNSI along with the surrounding Fe aqueous solution entered the cells. Under TEM, many carbon nanoparticles were identified in the cytoplasm rather than in the nucleus (Figure 5). The size and shape of these particles were identical to those of CNSI–Fe. These particles were in the phagocytotic vesicles, and the cells lost the intact membrane.

To further verify the accumulation of CNSI–Fe in the tumor, we quantified ^{13}C-CNSI by IRMS and Fe by ICP-OES at 1 day postinjection (Figure 6). Upon intratumoral injection, most CNSI particles and Fe were detected in the tumor. There was no meaningful increase of both in other tissues. About 56% of the injected dose for Fe was trapped in the tumor. The remaining 44% entered the blood circulation and was well balanced by the body, so no Fe increase was found. The steady Fe concentrations in other tissues were important for the biosafety of CNSI–Fe. There was about 900 μg of Fe in mouse blood circulation, and the Fe released into the blood was only 60 μg, so the unchanged Fe was not surprising. Fe accumulation in the tumor was relatively stable. After 14 days, the Fe concentration in the tumor of the CNSI–Fe-treated group was still nearly 9 times higher than that that of the control group. In addition, the distribution patterns of CNSI and Fe were quite different upon intravenous injection of CNSI–Fe. The main accumulation organ was the liver, and there was no tumor accumulation.

Amplified Oxidative Stress. The accumulation of Fe in the tumor led to strong oxidative stress (Figure 7). First, we identified the $^{\bullet}$OH radicals in tumor tissues at 1 day after the treatment. CNSI–Fe induced twice the amount of $^{\bullet}$OH radicals in the tumor compared to Fe^{2+} alone. There was no $^{\bullet}$OH radical found in CNSI-exposed group and the control group. Similar generation of $^{\bullet}$OH radicals by CNSI–Fe treatment was also observed in in vitro assessment, which led to the proliferation inhibition of H22 cells (Figure S5). Efficient generation of $^{\bullet}$OH radicals led to serious oxidative stress. Both Fe^{2+} and CNSI–Fe induced the increase of H_2O_2 and malondialdehyde (MDA) at 1 day. A slight decrease of glutathione (GSH) was observed in the CNSI–Fe-treated group. The oxidative stress remained to 14 days. Significant increases were found for H_2O_2, peroxidase (POD), MDA, and GSH in the CNSI–Fe-exposed group. Only MDA increased in the Fe(II) group. No significant change was found in the CNSI and control groups.

Low Toxicity of CNSI–Fe. The low toxicity of CNSI–Fe was evidenced by multiple techniques after intratumoral injection (Figure 8). First, the bodyweight increase of the CNSI–Fe-treated group (CNSI–Fe L group) was similar to that of the control group. Further increasing the dosages led to weight gain inhibition (CNSI–Fe M group and CNSI–Fe H group). The Fe(II) group induced a statistically significant

https://dx.doi.org/10.1021/acsami.0c07617
ACS Appl. Mater. Interfaces 2020, 12, 29094–29102

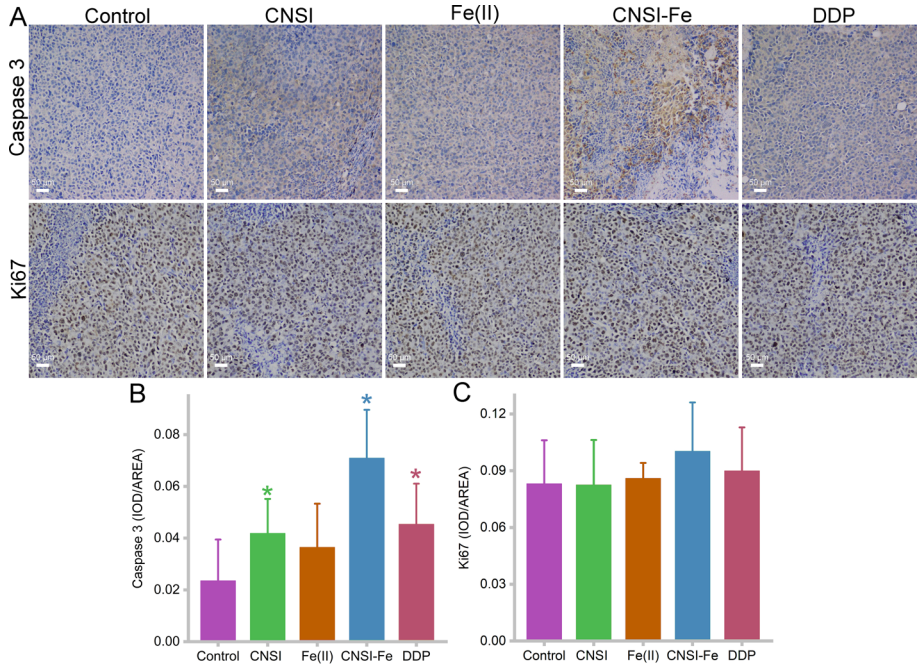

Figure 3. Immunohistochemistry of tumor tissues. (A) Representative images of immunohistochemical analyses. (B) Caspase 3 level changes. (C) Ki67 level changes. (*) $p < 0.05$ compared with the control group ($n = 3$).

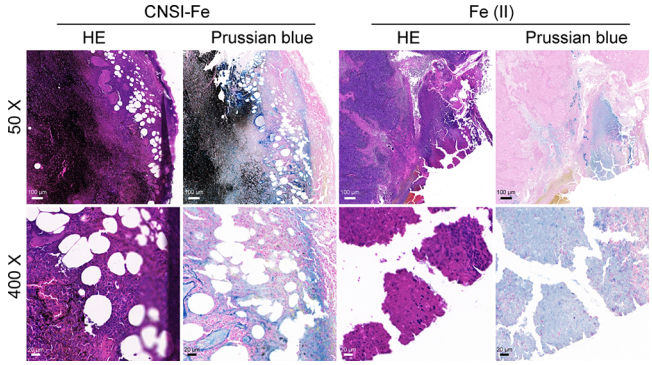

Figure 4. Visualization of Fe accumulation in tumor cells after injection of CNSI−Fe and Fe(II).

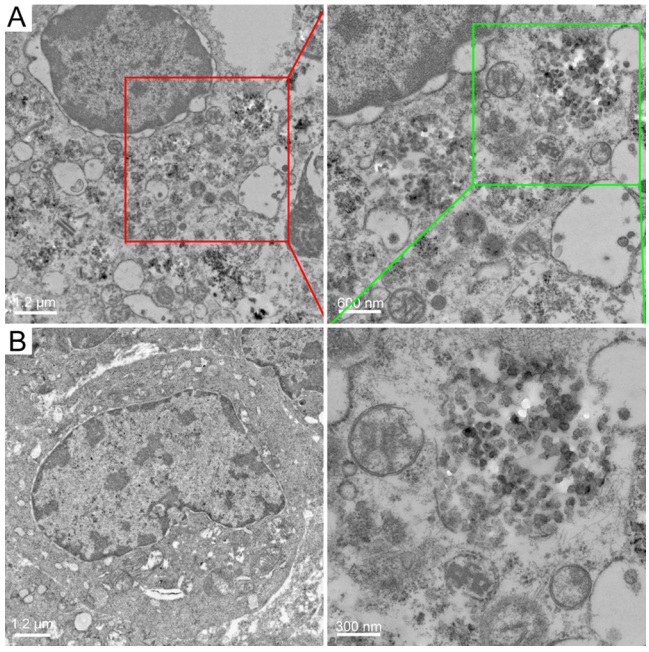

Figure 5. TEM visualization of CNSI−Fe in the tumor. (A) TEM image of the CNSI−Fe-treated tumor. (B) TEM image of the tumor in the control group.

weight gain inhibition at 11 days. The CNSI group induced growth inhibition at 4 days. The serum biochemistry parameters were all unchanged upon injection of a low dosage of CNSI−Fe (CNSI−Fe L group) at 14 days, except for a small increase of the creatinine (Cr) level. Higher dosages led to decreases of the aminotransferase (AST), alanine aminotransferase (ALT), and lactate dehydrogenase (LDH) levels in the CNSI−Fe M group and CNSI−Fe H group, indicating meaningful hepatic damage. The aspartate aminotransferase (ALP) level increased in the CNSI−Fe M group and CNSI−Fe H group, also suggesting the hepatic toxicity. For hematological measurements, three statistically significant changes were observed, namely, hemoglobin (HGB) of the CNSI−Fe L group, platelet (PLT) of the CNSI−Fe H group, and lymphocyte (Lymph) of the Fe(II) group. In the histopathological observations, the liver and spleen kept the typical structure in the control group (Figure 8D). Slight inflammation was observed in the liver in all groups (red arrows). In the CNSI−Fe L group, there were some swollen and vacuolated hepatic cells observed (yellow arrow). In the CNSI−Fe M and CNSI−Fe H groups, the swollen and vacuolated hepatic cells became dominating. The spleen kept the normal structure, except that more apoptotic bodies (green arrows) were found in the CNSI−Fe M and CNSI−Fe H groups. Other organs, including the heart, lung, and kidneys, also showed the normal structure after injection of CNSI−Fe.

DISCUSSION

In the aforementioned experiments, we observed the competitive performance of CNSI−Fe in treating tumors compared to DDP. The combination of CNSI and Fe is critical

https://dx.doi.org/10.1021/acsami.0c07617
ACS Appl. Mater. Interfaces 2020, 12, 29094−29102

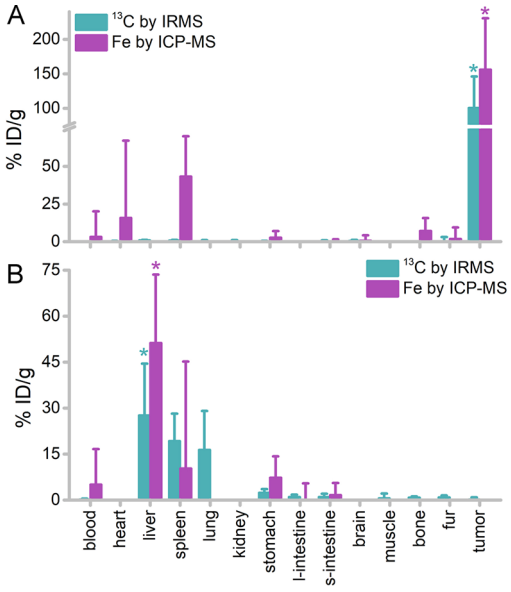

Figure 6. Quantification of CNSI−Fe in tissues. (A) Intratumoral injection. (B) Intravenous injection. (*) $p < 0.05$ compared with the control group ($n = 5$).

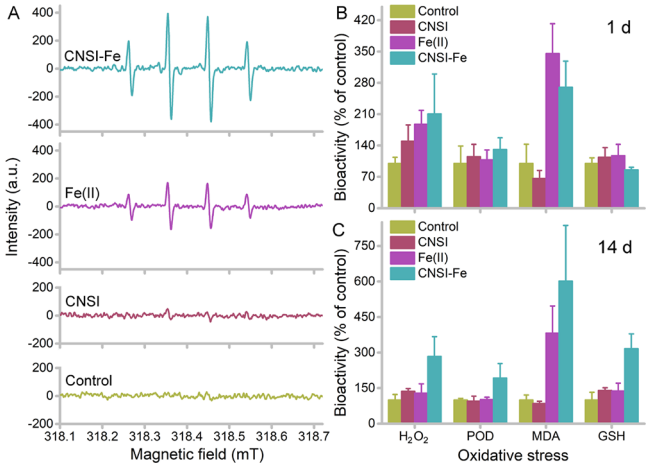

Figure 7. Oxidative stress of a CNSI−Fe-treated tumor. (A) ESR spectra at 1 day. (B) Oxidative stress of tumor tissues at 1 day. (C) Oxidative stress of tumor tissues at 14 days.

for this purpose, because single use of CNSI or Fe was not efficient in tumor growth inhibition. The mechanism of CNSI−Fe for cancer therapy was the strong ROS generation, which consequently induced oxidative damage to tumor tissue. Therefore, CNSI−Fe was very hopeful in tumor inhibition with high efficiency and low toxicity.

The efficient tumor inhibition of CNSI−Fe should be attributed to the synergistic effects of both CNSI and Fe^{2+}. In our study, a separate dosage of CNSI or Fe(II) only resulted in no or low efficiency of tumor inhibition (Figure S3). CNSI was a biocompatible carbon material, which did not arouse oxidative stress, so the lack of therapeutic effect was reasonable.[23] Fe^{2+} was toxic and efficient in catalyzing H_2O_2 decomposition. However, when Fe^{2+} was directly injected to the tumor, Fe^{2+} hardly migrated into the cytoplasm due to the limited amount of transferrin and other transporters.[2,3] Typically, tumor cells have several Fe uptake pathways, such as Tf-Fe2/TfR, Zrt- and Irt-like protein 14 (zip14), Zrt- and Irt-like protein 8 (zip8), divalent metal transporter 1 (DMT-1), and lipocalin2 (LCN2)/LCN2 receptor (LCN2R) (Figure S6). These pathways depend on the amount of transporters and receptors and thus would not actively take too many Fe ions in a short time. The overdosed Fe would stay outside the cell membrane. Fe^{2+} ions would slowly migrate along with blood circulation to leave the tumor. Therefore, the efficiency of Fe^{2+} was much lower than that of CNSI−Fe. For CNSI−Fe, the formulation took advantage of both CNSI and Fe. The cells would take the CNSI particles by endocytosis.[24,25] The endocytosis of CNSI was visualized by the TEM observations of ultrathin sections of tumor tissues (Figure 5A). The adsorbed Fe^{2+} on carbon nanoparticles and surrounding Fe^{2+} solution would be swallowed together. This led to the overwhelming dosage of Fe^{2+} in the cytoplasm. Due to the blocking of the FPN pathway in tumor cells (Figure S6), the cells could not pump out Fe^{2+} and the accumulation of Fe^{2+} lasted for a long time, which was consistent with the ICP-OES measurements. The accumulation of Fe^{2+} was proven by the Prussian blue staining (Figure 3) and the ICP-OES measurements (Figure 5A). The similar distribution patterns of CNSI and Fe confirmed the hypothesis that Fe^{2+} took the ride of CNSI to enter the tumor. After entering the cytoplasm, the intracellular Fe^{2+} catalyzed the decomposition of H_2O_2 to generate hydroxyl radicals that attacked the tumor cells and the cellular structure was destroyed (Scheme 1). The delivery of Fe^{2+} by CNSI into cells was reasonable, and such delivery systems based on nanomaterials were widely reported in the literature.[25−28] For example, we reported that CNSI could deliver doxorubicin (DOX) into cancer cells for therapy purposes.[25] The other drug delivery systems of carbon nanotubes, graphene and carbon dots, have been well established, taking advantage of the endocytosis of these carbon nanomaterials.[26−28] In addition, it should be noted that the hydrodynamic radii of CNSI−Fe were around 190 nm, a suitable size for endocytosis according to the literature.[29]

The mechanism of CNSI−Fe for cancer therapy was the Fenton reaction in vivo to generate hydroxyl radicals. In our study, we verified the mechanism of CNSI−Fe treatment by ESR spectra. CNSI−Fe induced strong hydroxyl radical generation, which was more than twice that of the Fe^{2+}-treated group (Figures 7 and S5). CNSI as a benign reagent did not arouse hydroxyl radical production.[22] However, according to our previous reports, elemental carbon could facilitate the Fenton reaction and played a sacrificial role in regenerating Fe^{2+} as a reducer.[30] Without CNSI, the Fenton reaction should be less effective and harder to regenerate at pH higher than 3. As a consequence of the in vivo Fenton reaction, the hydroxyl radicals initiated the oxidative stress in tumor tissues. At day 1 postinjection, CNSI−Fe led to the increase of H_2O_2 and MDA accompanied by the depletion of GSH. The Fe^{2+}-treated group only showed H_2O_2 and MDA increases, but the depletion of GSH was not significant. The generation of ROS to modify the TME is crucial for tumor inhibition. In the literature, different formulations of Fe and Mn were used for the Fenton reaction to generate hydroxyl radicals.[30−32] In these studies, the hydroxyl radicals were regarded as the main reason for tumor inhibition. Compared to the use of Fe- and Mn-containing nanoparticles, CNSI−Fe had a simple formulation, easy preparation, and fast radical generation, so CNSI−Fe could be ranking among the most promising ROS generation reagents for cancer therapy. Beyond the change of TME, according to the literature, the Fe accumulation, lipid

https://dx.doi.org/10.1021/acsami.0c07617
ACS Appl. Mater. Interfaces 2020, 12, 29094−29102

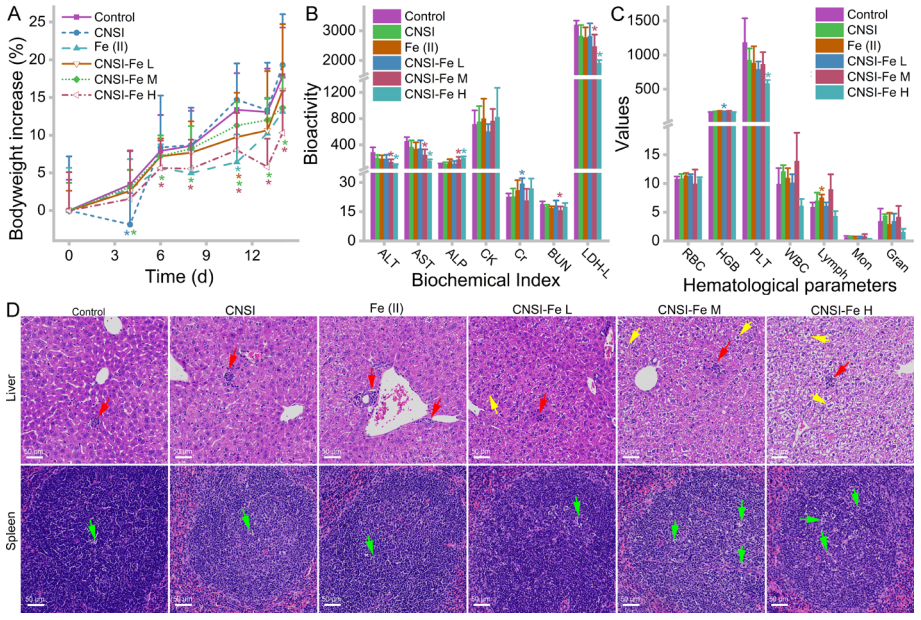

Figure 8. Toxicity evaluations of CNSI−Fe. (A) Bodyweight. (B) Serum biochemistry. (C) Hematology. (D) HE images. (*) $p < 0.05$ compared with the control group ($n = 5$). Inflammation is indicated by red arrows, swollen and vacuolated hepatic cells are indicated by yellow arrows, and apoptotic bodies are indicated by green arrows.

Scheme 1. Schematic Illustration of the Fenton Reaction in the Tumor upon Injection of CNSI−Fe

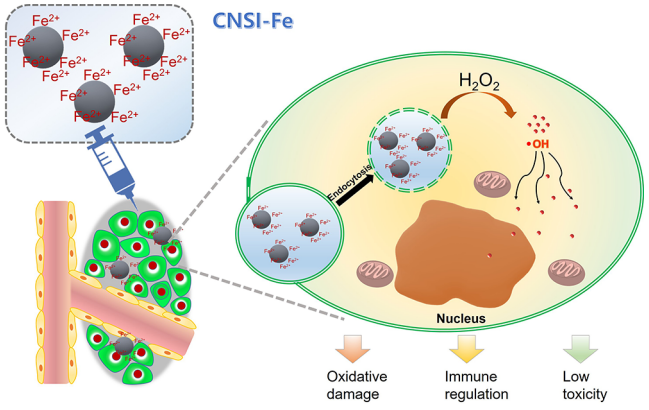

peroxidation and glutathione depletion should simultaneously occur during ferroptosis.[33] Additional evidence of ferroptosis was the apoptosis of tumor cells, since a significant increase of caspase 3 in the CNSI−Fe group was observed (Figure 3). Thus, CNSI−Fe might be capable of initiating ferroptosis, while Fe^{2+} was not. This could be regarded as a downstream event of the Fenton reaction in the tumor. In fact, the ferroptosis has been applied in tumor inhibition using Fe-containing nanoparticles as the catalysts.[34,35]

The limiting translocation of CNSI−Fe in the body was the main reason for its low toxicity. In our study, the low toxicity of CNSI−Fe was evidenced by multiple techniques, which is crucial for clinical applications of in the area of nanomedicine. Previously, we demonstrated that high dosages of CNSI into the blood circulation did not induce toxicity to mice.[22] More than 100 000 patients receive the intratumoral injection of CNSI every year, and the good biocompatibility of CNSI was proven during these clinical applications. CNSI−Fe was intratumorally injected to mice, and the quantification data by IRMS and ICP-OES indicated that the main portions of CNSI and Fe were trapped in tumor tissues. No significant increase of CNSI or Fe was found in other tissues. Therefore, direct damage of CNSI−Fe to normal tissues was not possible. The toxicity of CNSI−Fe to normal tissues could only occur through indirect pathways, e.g., the passing of ROS from the tumor to normal tissues through blood circulation. The possibility of indirect damage was very low, so the toxicity of CNSI−Fe was not observed at the current concentration. In our pre-evaluations, 50 μL of free Fe ions (24 mg Fe/mL) would lead to the death of mice and the value was 27 mg Fe/mL for CNSI−Fe, implying that CNSI−Fe helped in trapping Fe ions. The lethal concentration of CNSI−Fe was much higher than the effective concentration here, so CNSI−Fe was safe for in vivo treatments. The detoxification of Fe by CNSI was also reasonable, and a similar phenomenon has been widely reported in the literature.[25−27] Previously, we showed that DOX loaded on CNSI was less toxic than free DOX, while the therapeutic efficiency was not changed.[25] Carbon nanomaterials were reported to adsorb metal ions with a large quantity.[36] The fixation of metal ions alleviates the toxicity to cells and animals.

For clinical applications, CNSI−Fe is encouraged for use before surgery. First, many patients are now receiving CNSI before oncological surgery for tumor drainage lymph node mapping.[37,38] The doctors are well trained and experienced in intratumoral injection. By changing CNSI into CNSI−Fe, the injection protocol is identical. There is no practical difficulty for doctors to use CNSI−Fe. Second, CNSI−Fe still has the ability to stain the lymph node black (Figure S7). Upon intratumoral injection, the patients would receive two benefits, including tumor inhibition and lymph node mapping. The black color of CNSI−Fe would guide the injection and oncological surgery. Third, the injected CNSI−Fe would be dissected during surgery; therefore, there is unlikely to be long-term toxicity. Thus, the good biosafety of CNSI−Fe is expected. Fourth, during the clinical treatments, when the tumor is too big, the therapeutic efficiency of oncological

https://dx.doi.org/10.1021/acsami.0c07617
ACS Appl. Mater. Interfaces 2020, 12, 29094−29102

surgery would be low. Injection of CNSI−Fe could shrink the tumor to enhance the efficiency, narrow the wound, and weaken the ability of the tumor to infiltrate the surrounding area. Preoperative reduction of the tumor with CNSI−Fe would have the same effect of the neoadjuvant chemotherapy; thus, CNSI−Fe treatment might be applied as an alternative therapy of neoadjuvant chemotherapy. Fifth, the accumulation of CNSI−Fe in draining lymph nodes might be useful in the inhibition of local lymph node metastasis. In this regard, CNSI−Fe is very hopeful for clinical applications with multiple benefits.

CONCLUSIONS

In summary, carbon nanoparticles loaded with Fe^{2+} showed high antitumor activity upon intratumoral injection to mice, where the arousal of extensive ROS was the main mechanism. Intratumoral-injected CNSI−Fe was largely retained in the tumor tissue to increase the Fe content sharply to achieve competitive antitumor activity to the classical antitumor drug DDP. The hydroxyl radicals were continuously generated in tumor tissues during the 14-day observation period, and meaningful oxidative damage was induced. Meanwhile, because Fe and CNSI were strictly trapped in the tumor, the levels of both did not change in other tissues. The unchanged Fe levels in the body ensured the low toxicity of CNSI−Fe. This study highlights the potential use of essential element Fe as an antitumor drug with the help of carbon nanoparticles. It is hoped that our results would stimulate more clinical applications of CNSI−Fe in theranostics and benefit the development of nanomaterials for cancer therapy.

MATERIALS AND METHODS

Preparation of CNSI−Fe and ^{13}C-CNSI−Fe. A 0.8043 g amount of PVP was ground in 4 mL of water and added with 2.026 g of C40 carbon powder. The mixture was ground for 1.5 h with 2 mL of water, adding after 30 min. A black gel-like sample was transferred to a beaker and added with 30 mL of water. The pH value was adjusted to pH 6 with sodium citrate solution. The black suspension was further homogenized at 25 000 rpm for 10 min 5 times to produce CNSI. For ^{13}CNSI, the raw material ^{13}C-ash was prepared by the arc discharge method kindly by Prof Xue-Ling Chang. A 0.5157 g amount of PVP was ground in 2.5 mL of water and added with 1.258 g of ^{13}C-ash. The mixture was ground for 1.5 h with 1 mL of water added after 30 min. A black gel-like sample was transferred to a beaker and added with 19.5 mL of water. The pH adjustment and homogenization was performed following the same protocol. The ^{13}C content of ^{13}CNSI was analyzed by IRMS ((DELTA V Advantage, Thermo Electron-Finnigan, USA). To prepare CNSI−Fe and ^{13}C-CNSI−Fe, the CNSI suspension (50 mg carbon particles/mL) was mixed with 5.5 mg Fe/mL $FeSO_4$ aqueous solution at a 1:1 volume ratio under sonication and then lyophilized. Both normal and labeled CNSI−Fe were carefully characterized by TEM (Autoflex, Bruker, Bonn, Germany), high-resolution TEM (HRTEM, Tecnai G2 20, FEI, USA), DLS (Zetasizer Nano ZS90, Malvern Instruments, Malvern, UK), Raman spectroscopy (Renishaw inVia plus, Renishaw, Wotton-under-Edge, UK), XPS (Axis Ultra, Kratos, Manchester, UK), elemental analysis (Vario EL, Elementar, Germany), and IR (Tensor27, Bruker, Germany) before use. The C 1s spectrum was subjected to CasaXPS software using the automatic fitting protocol. The Fe^{2+} content was measured by the *o*-phenanthroline method, and the total Fe content was determined by ICP-OES.

Tumor Inhibition Evaluation. The ascites of H22 tumor-bearing mice (BALB/c mice) were collected and adjusted to 3×10^7 cells/mL. The animal experiments were approved by the Animal Centre of Southwest Minzu University and performed in accordance with the Animal Care and Use Program Guidelines of the Sichuan Province, China. Each mouse was injected with 0.1 mL of ascites on the right upper limb. The mice were randomly grouped into 5 mice each when the tumors reached 100 mm^3. Five groups were injected with saline (control group, 50 μL by intratumoral injection), DDP (DDP group, 5 mg/kg by intraperitoneal injection), CNSI (CNSI group, 58 mg C/kg by intratumoral injection), $FeSO_4$ [Fe(II) group, 6.3 mg Fe/kg by intratumoral injection], and CSNI-Fe (CNSI−Fe group, 58 mg C/kg and 6.3 mg Fe/kg by intratumoral injection) at day 0 and day 3. In our pre-evaluations, higher dosages (116 mg C/kg + 6.3 mg Fe/kg, 58 mg C/kg + 12.6 mg Fe/kg, and 116 mg C/kg + 12.6 mg Fe/kg) showed very limited increases in tumor inhibition. Thus, to avoid the unwanted toxicity, we adopted 58 mg C/kg + 6.3 mg Fe/kg. The tumor volumes were recorded. After 14 days, the mice were sacrificed and the tumors were dissected for weighting. The tumors were fixed by 10% formaldehyde solution and continuously sliced for HE staining and Prussian blue staining following standard protocols. The tumors were fixed by 3% glutaraldehyde for TEM observations following the previous protocols.[39] The tumors were fixed by 10% formaldehyde solution and sent to Wuhan Servicebio Technology Co. for immunohistochemical analyses of caspase 3 and Ki67. The immunohistochemical slices were analyzed by measuring the areal densities. For each slice, 3 replicate fields were recorded. The images were analyzed by Image-Pro Plus 6.0 software (Media Cybernetics, Inc.). The areal density was calculated by IOD/AREA, where IOD is the integrated optical density and AREA is the pixel area.

To evaluate the biodistribution of CNSI−Fe, mice were injected with ^{13}C-CNSI−Fe and the tissues were collected at 1 day and 14 days. The ^{13}C contents were analyzed by IRMS following our previous protocols.[23] For Fe detection, tissues were digested with 10 mL of HNO_3 and 3 mL of H_2O_2 in an automatic microwave. The tissue samples were soaked in a HNO_3/H_2O_2 mixture for 12 h and digested at 190 °C for 1 h. The as-obtained solution was measured by ICP-OES.

Oxidative Stress Assays. The tumor tissues were collected from tumor inhibition experiments at 1 day and 14 days postinjection, including the saline group, CNSI group, Fe^{2+} group, and CNSI−Fe group. The tissues were homogenized to obtain 10% homogenates. The H_2O_2, POD, MDA, and GSH levels were measured strictly following the recommended protocols of the kits (Nanjing Jiancheng Bioengineering Institute, China). Separately, the homogenates of tumor tissues were added with 5,5-dimethyl-1-pyrroline-*N*-oxide (DMPO), and the ESR spectra were recorded to reflect the contents of hydroxyl radicals (JES-FA200, JEOL, Japan).

Toxicological Evaluations. CNSI−Fe (58 mg C/kg bodyweight + 6.3 mg Fe/kg bodyweight as the CNSI−Fe L group, 58 mg C/kg bodyweight + 31.5 mg Fe/kg bodyweight as the CNSI−Fe M group, and 58 mg C/kg bodyweight + 50.4 mg Fe/kg bodyweight as the CNSI−Fe H group), $FeSO_4$ (6.3 mg Fe/kg bodyweight), CNSI (58 mg C/kg bodyweight), and saline were intratumorally injected to BALB/c mice separately for toxicity evaluations. The bodyweights were recorded three times per week. After 14 days, the whole blood samples were collected for hematological analyses (Chemray 240, Rayto, China), including red blood cell (RBC), HGB, PLT, white blood cell (WBC), Lymph, monocytes (Mon), and neutrophilic granulocyte (Gran). The serum samples were collected for biochemical analyses (Chemray 240, Rayto, China), including aspartate AST, ALT, ALP, creatine kinase (CK), Cr, blood urine nitrogen (BUN), and LDH. The liver and spleen tissues, including the heart, liver, spleen, kidneys, and lung, were dissected, fixed in 10% formaldehyde solution for standard HE staining, and checked under an optical microscope (Eclipse CI, Nikon, Japan).

Statistical Analysis of Experimental Data. All data were analyzed as the mean with the standard deviation (mean ± SD). The significance was calculated using the student-*t* test. Differences were considered significant at $p < 0.05$.

https://dx.doi.org/10.1021/acsami.0c07617
ACS Appl. Mater. Interfaces 2020, 12, 29094−29102

■ ASSOCIATED CONTENT

Supporting Information

The Supporting Information is available free of charge at https://pubs.acs.org/doi/10.1021/acsami.0c07617.

In vitro experimental protocols, schematic illustration of the CNSI preparation protocol, HRTEM image of CNSI−Fe and ^{13}C-CNSI−Fe, antitumor activity of CNSI and Fe(II), Prussian blue staining images of CNSI and saline-injected tumors, in vitro antitumor activity of CNSI−Fe, schematic illustration of Fe transportation in cancer cells, imaging of the tumor drainage lymph nodes by CNSI−Fe (PDF)

■ AUTHOR INFORMATION

Corresponding Authors

Sheng-Tao Yang − *College of Chemistry and Environment Protection Engineering, Southwest Minzu University, Chengdu 610041, People's Republic of China;* orcid.org/0000-0001-6795-8879; Phone: +86-28-85522269; Email: yangst@pku.edu.cn

Xiaohai Tang − *Sichuan Enray Pharmaceutical Sciences Company, Chengdu 610041, People's Republic of China;* Phone: +86-28-8550-3335; Email: pharmmateceo@aliyun.com

Authors

Ping Xie − *State Key Laboratory of Oral Diseases, West China College of Stomatology, Sichuan University, Chengdu 610041, People's Republic of China*

Yuanfang Huang − *Sichuan Enray Pharmaceutical Sciences Company, Chengdu 610041, People's Republic of China*

Cheng Zeng − *Sichuan Enray Pharmaceutical Sciences Company, Chengdu 610041, People's Republic of China*

Qian Xin − *Sichuan Enray Pharmaceutical Sciences Company, Chengdu 610041, People's Republic of China*

Guangfu Zeng − *Sichuan Enray Pharmaceutical Sciences Company, Chengdu 610041, People's Republic of China*

Shengnan Yang − *College of Chemistry and Environment Protection Engineering, Southwest Minzu University, Chengdu 610041, People's Republic of China*

Pingfang Xia − *Sichuan Enray Pharmaceutical Sciences Company, Chengdu 610041, People's Republic of China*

Kexin Tang − *Sichuan Enray Pharmaceutical Sciences Company, Chengdu 610041, People's Republic of China*

Complete contact information is available at: https://pubs.acs.org/10.1021/acsami.0c07617

Notes

The authors declare the following competing financial interest(s): Y.F.H., C.Z., Q.X., G.F.Z., P.F.X. and X.H.T. are the employees of Sichuan Enray Pharmaceutical Sciences Company. K.X.T. is a research participant from Chengdu No. 7 High School in Sichuan Enray Pharmaceutical Sciences Company.

■ ACKNOWLEDGMENTS

We are grateful to Prof. Xue-Ling Chang at High Energy Physics, CAS, for preparation ^{13}C-ash by the arc discharge method. This work was financially supported by the National Natural Science Foundation of China (No. 21777132), the Major Drug Discovery Science and Technology Major Projects of 12th Five-Year National Plan and Research Fund for Major Drug Research of Nation Science and Technology (863 Projects, 2012ZX091021041 and 2012ZX09102101-015), and the National Program for Support of Top-notch Young Professionals.

■ REFERENCES

(1) Mertz, W. The Essential Trace Elements. *Science* **1981**, *213*, 1332−1338.

(2) Gkouvatsos, K.; Papanikolaou, G.; Pantopoulos, K. Regulation of Iron Transport and the Role of Transferrin. *Biochim. Biophys. Acta, Gen. Subj.* **2012**, *1820*, 188−202.

(3) Drakesmith, H.; Nemeth, E.; Ganz, T. Ironing out Ferroportin. *Cell Metab.* **2015**, *22*, 777−787.

(4) Bokare, A. D.; Choi, W. Review of Iron-Free Fenton-like Systems for Activating H_2O_2 in Advanced Oxidation Processes. *J. Hazard. Mater.* **2014**, *275*, 121−135.

(5) Eid, R.; Arab, N. T. T.; Greenwood, M. T. Iron Mediated Toxicity and Programmed Cell Death: A Review and a Re-examination of Existing Paradigms. *Biochim. Biophys. Acta, Mol. Cell Res.* **2017**, *1864*, 399−430.

(6) Arami, H.; Khandhar, A.; Liggitt, D.; Krishnan, K. M. In Vivo Delivery, Pharmacokinetics, Biodistribution and Toxicity of Iron Oxide Nanoparticles. *Chem. Soc. Rev.* **2015**, *44*, 8576−8607.

(7) Joyce, J. A.; Pollard, J. W. Microenvironmental Regulation of Metastasis. *Nat. Rev. Cancer* **2009**, *9*, 239−252.

(8) Han, X.; Li, Y.; Xu, Y.; Zhao, X.; Zhang, Y.; Yang, X.; Wang, Y.; Zhao, R.; Anderson, G. J.; Zhao, Y.; Nie, G. Reversal of Pancreatic Desmoplasia by Re-educating Stellate Cells with a Tumour Microenvironment Activated Nanosystem. *Nat. Commun.* **2018**, *9*, 3390.

(9) Zhao, P.; Ren, S.; Liu, Y.; Huang, W.; Zhang, C.; He, J. PL-$W_{18}O_{49}$-TPZ Nanoparticles for Simultaneous Hypoxia-Activated Chemotherapy and Photothermal Therapy. *ACS Appl. Mater. Interfaces* **2018**, *10*, 3405−3413.

(10) Gao, R.; Mitra, R. N.; Zheng, M.; Wang, K.; Dahringer, J. C.; Han, Z. Developing Nanoceria-based pH-dependent Cancer-directed Drug Delivery System for Retinoblastoma. *Adv. Funct. Mater.* **2018**, *28*, 1806248.

(11) Xia, D.; Xu, P.; Luo, X.; Zhu, J.; Gu, H.; Huo, D.; Hu, Y. Overcoming Hypoxia by Multistage Nanoparticle Delivery System to Inhibit Mitochondrial Respiration for Photodynamic Therapy. *Adv. Funct. Mater.* **2019**, *29*, 1807294.

(12) Yu, B.; Wei, H.; He, Q.; Ferreira, C. A.; Kutyreff, C. J.; Ni, D.; Rosenkrans, Z. T.; Cheng, L.; Yu, F.; Engle, J. W.; Lan, X.; Cai, W. Efficient Uptake of ^{177}Lu-porphyrin-PEG Nanocomplexes by Tumor Mitochondria for Multimodal-Imaging-Guided Combination Therapy. *Angew. Chem., Int. Ed.* **2018**, *57*, 218−222.

(13) Huo, M.; Wang, L.; Chen, Y.; Shi, J. Tumor-selective Catalytic Nanomedicine by Nanocatalyst Delivery. *Nat. Commun.* **2017**, *8*, 357.

(14) Fontecave, M.; Pierre, J. L. Iron: Metabolism, Toxicity and Therapy. *Biochimie* **1993**, *75*, 767−773.

(15) Tang, Z.; Liu, Y.; He, M.; Bu, W. Chemodynamic Therapy: Tumour Microenvironment-mediated Fenton and Fenton-like Reaction. *Angew. Chem., Int. Ed.* **2019**, *58*, 946−956.

(16) Liu, Y.; Zhen, W.; Wang, Y.; Liu, J.; Jin, L.; Zhang, T.; Zhang, S.; Zhao, Y.; Song, S.; Li, C.; Zhu, J.; Yang, Y.; Zhang, H. One-dimensional Fe_2P Acts as a Fenton Agent in Response to NIR II Light and Ultrasound for Deep Tumor Synergetic Theranostics. *Angew. Chem., Int. Ed.* **2019**, *58*, 2407−2412.

(17) Gao, S.; Lin, H.; Zhang, H.; Yao, H.; Chen, Y.; Shi, J. Nanocatalytic Tumor Therapy by Biomimetic Dual Inorganic Nanozyme-catalyzed Cascade Reaction. *Adv. Sci.* **2019**, *6*, 1801733.

(18) Wu, H.; Cheng, K.; He, Y.; Li, Z.; Su, H.; Zhang, X.; Sun, Y.; Shi, W.; Ge, D. Fe_3O_4-based Multifunctional Nanospheres for Amplified Magnetic Targeting Photothermal Therapy and Fenton Reaction. *ACS Biomater. Sci. Eng.* **2019**, *5*, 1045−1056.

(19) Huang, G.; Chen, H.; Dong, Y.; Luo, X.; Yu, H.; Moore, Z.; Bey, E. A.; Boothman, D. A.; Gao, J. Superparamagnetic Iron Oxide

Nanoparticles: Amplifying ROS Stress to Improve Anticancer Drug Efficacy. *Theranostics* **2013**, *3*, 116−126.
(20) Yin, S.; Song, G.; Yang, Y.; Zhao, Y.; Wang, P.; Zhu, L.; Yin, X.; Zhang, X. Persistent Regulation of Tumor Microenvironment via Circulating Catalysis of $MnFe_2O_4$@Metal−organic Frameworks for Enhanced Photodynamic Therapy. *Adv. Funct. Mater.* **2019**, *29*, 1901417.
(21) Li, Z.; Ao, S.; Bu, Z.; Wu, A.; Wu, X.; Shan, F.; Ji, X.; Zhang, Y.; Xing, Z.; Ji, J. Clinical Study of Harvesting Lymph Nodes with Carbon Nanoparticles in Advanced Gastric Cancer: A Prospective Randomized Trial. *World J. Surg. Oncol.* **2016**, *14*, 88.
(22) Xie, P.; Xin, Q.; Yang, S.-T.; He, T.; Huang, Y.; Zeng, G.; Ran, M.; Tang, X. Skeleton Labeled ^{13}C-carbon Nanoparticles for the Imaging and Quantification in Tumor Drainage Lymph Nodes. *Int. J. Nanomed.* **2017**, *12*, 4891−4899.
(23) Xie, P.; Yang, S.-T.; He, T.; Yang, S.; Tang, X. Bioaccumulation and Toxicity of Carbon Nanoparticles Suspension Injection in Intravenously Exposed Mice. *Int. J. Mol. Sci.* **2017**, *18*, 2562.
(24) Yan, G.; Song, Z.; Liu, Y.; Su, Q.; Liang, W.; Cao, A.; Sun, Y.; Wang, H. Effects of Carbon Dots Surface Functionalities on Cellular Behaviors: Mechanistic Exploration for Opportunities in Manipulating Uptake and Translocation. *Colloids Surf., B* **2019**, *181*, 48−57.
(25) Huang, Y.; Xie, P.; Yang, S.-T.; Zhang, X.; Zeng, G.; Xin, Q.; Tang, X. Carbon Nanoparticles Suspension Injection for the Delivery of Doxorubicin: Comparable Efficacy and Reduced Toxicity. *Mater. Sci. Eng., C* **2018**, *92*, 416−423.
(26) Mahajan, S.; Patharkar, A.; Kuche, K.; Maheshwari, R.; Deb, P. K.; Kalia, K.; Tekade, R. K. Functionalized Carbon Nanotubes as Emerging Delivery System for the Treatment of Cancer. *Int. J. Pharm.* **2018**, *548*, 540−558.
(27) Liu, J.; Dong, J.; Zhang, T.; Peng, Q. Graphene-based Nanomaterials and Their Potentials in Advanced Drug Delivery and Cancer Therapy. *J. Controlled Release* **2018**, *286*, 64−73.
(28) LeCroy, G. E.; Yang, S.-T.; Yang, F.; Liu, Y.; Fernando, K. A. S.; Bunker, C. E.; Hu, Y.; Luo, P. G.; Sun, Y.-P. Functionalized Carbon Nanoparticles: Syntheses and Applications in Optical Bioimaging and Energy Conversion. *Coord. Chem. Rev.* **2016**, *320−321*, 66−81.
(29) Sahay, G.; Alakhova, D. Y.; Kabanov, A. V. Endocytosis of Nanomedicines. *J. Controlled Release* **2010**, *145*, 182−195.
(30) Sun, C.; Yang, S.-T.; Gao, Z.; Yang, S.; Yilihamu, A.; Ma, Q.; Zhao, R.; Xue, F. Fe_3O_4/TiO_2/Reduced Graphene Oxide Composites as Highly Efficient Fenton-like Catalyst for the Decoloration of Methylene Blue. *Mater. Chem. Phys.* **2019**, *223*, 751−757.
(31) Liu, X.; Sun, C.; Chen, L.; Yang, H.; Ming, Z.; Bai, Y.; Feng, S.; Yang, S.-T. Decoloration of Methylene Blue by Heterogeneous Fenton-like Oxidation on Fe_3O_4/SiO_2/C Nanospheres in Neutral Environment. *Mater. Chem. Phys.* **2018**, *213*, 231−238.
(32) Xu, Z.; Qin, L.; Zhang, Y.; Li, X.; Nan, J.; Guo, X.; Zhang, G. In-situ Green Assembly of Spherical Mn-based Metal-organic Composites by Ion Exchange for Efficient Electrochemical Oxidation of Organic Pollutant. *J. Hazard. Mater.* **2019**, *369*, 299−308.
(33) Stockwell, B. R.; Friedmann Angeli, J. P.; Bayir, H.; Bush, A. I.; Conrad, M.; Dixon, S. J.; Fulda, S.; Gascon, S.; Hatzios, S. K.; Kagan, V. E.; Noel, K.; Jiang, X.; Linkermann, A.; Murphy, M. E.; Overholtzer, M.; Oyagi, A.; Pagnussat, G. C.; Park, J.; Ran, Q.; Rosenfeld, C. S.; Salnikow, K.; Tang, D.; Torti, F. M.; Torti, S. V.; Toyokuni, S.; Woerpel, K.A.; Zhang, D. D. Ferroptosis: A Regulated Cell Death Nexus Linking Metabolism, Redox Biology, and Disease. *Cell* **2017**, *171*, 273−285.
(34) Kim, S. E.; Zhang, L.; Ma, K.; Riegman, M.; Chen, F.; Ingold, I.; Conrad, M.; Turker, M. Z.; Gao, M.; Jiang, X.; Monette, S.; Pauliah, M.; Gonen, M.; Zanzonico, P.; Quinn, T.; Wiesner, U.; Bradbury, M. S.; Overholtzer, M. Ultrasmall Nanoparticles Induce Ferroptosis in Nutrient-Deprived Cancer Cells and Suppress Tumour Growth. *Nat. Nanotechnol.* **2016**, *11*, 977−985.
(35) Liu, M.; Liu, B.; Liu, Q.; Du, K.; Wang, Z.; He, N. Nanomaterial-induced Ferroptosis for Cancer Specific Therapy. *Coord. Chem. Rev.* **2019**, *382*, 160−180.
(36) Zhao, L.; Chen, J.; Xiong, N.; Bai, Y.; Yilihamu, A.; Ma, Q.; Yang, S.; Wu, D.; Yang, S.-T. Carboxylation as an Effective Approach to Improve the Adsorption Performance of Graphene Materials for Cu^{2+} Removal. *Sci. Total Environ.* **2019**, *682*, 591−600.
(37) Zhu, Y.; Chen, X.; Zhang, H.; Chen, L.; Zhou, S.; Wu, K.; Wang, Z.; Kong, L.; Zhuang, H. Carbon Nanoparticle-Guided Central Lymph Node Dissection in Clinically Node-Negative Patients with Papillary Thyroid Carcinoma. *Head Neck* **2016**, *38*, 840−845.
(38) Gu, J.; Wang, J.; Nie, X.; Wang, W.; Shang, J. Potential Role for Carbon Nanoparticles Identification and Preservation in situ of Parathyroid Glands during Total Thyroidectomy and Central Compartment Node Dissection. *Int. J. Clin. Exp. Med.* **2015**, *8*, 9640−9648.
(39) Tang, H.; Yang, S.-T.; Ke, D.; Yang, Y.; Liu, J.-H.; Chen, X.; Wang, H.; Liu, Y. Biological Behaviors and Chemical Fates of Ag_2Se Quantum Dots in vivo: Effect of Surface Chemistry. *Toxicol. Res.* **2017**, *6*, 693−704.

https://dx.doi.org/10.1021/acsami.0c07617
ACS Appl. Mater. Interfaces 2020, 12, 29094−29102